# Insights into enhanced activity and durability of hierarchical Fe-doped Ni(OH)$_2$/Ni catalysts for alkaline oxygen evolution reaction: In situ XANES studies

Sang-Yeon Lee [a], Hyun-Jung Oh [a], MinJoong Kim [b], Hyun-Seok Cho [b], Yong-Kul Lee [a,*]

[a] Laboratory of Advanced Catalysis for Energy and Environment, Department of Chemical Engineering, Dankook University, 152 Jukjeonro, Yongin 16892, South Korea
[b] Hydrogen Research Department, Korea Institute of Energy Research, 152 Gajungro, Daejeon 34129, South Korea

## ARTICLE INFO

## ABSTRACT

Nature of activation and degradation of NiFe layered double hydroxide (NiFe-LDH) and hierarchical Fe-doped Ni(OH)$_2$/Ni has been explored using in situ X-ray absorption near edge structure (XANES) spectroscopy coupled with cyclic voltammetry (CV) in a potential range of 0–0.9 V (vs. Hg/HgO). A series of NiFe-LDH samples have been prepared by electrodeposition with varying Ni/Fe molar ratios from 99:1–16:84. Fe has been doped on Ni(OH)$_2$ and anodized Ni as Fe-Ni(OH)$_2$ and Fe-ANi, respectively. CV and electrochemical impedance spectroscopy (EIS) analysis confirm the degradation of NiFe-LDH due to the redox irreversibility of Ni(OH)$_2$/NiOOH. On the other hand, hierarchical Fe-doped Ni(OH)$_2$/Ni shows not only high activity but also stability in alkaline OER. In situ XANES analysis demonstrated that the phase of Ni is maintained with Ni$^{2+}$ in Fe-ANi, while the phase of Ni$^{2+}$ changes to Ni$^{3.6+}$ in NiFe-LDH, contributing to durable OER performance of Fe-ANi even under potential fluctuations.

## 1. Introduction

Hydrogen is one of the most efficient energy carriers, which enables the storage of renewable energies from solar, tidal, and wind powers [1–6]. In this regard, the demand for hydrogen from water splitting using electrical power from renewable energy sources has increased [7–11]. Hydrogen and oxygen evolution reactions (HER, OER) occur at the cathode and the anode, respectively, in the electrolysis of water. Although the theoretical potential for water electrolysis is 1.23 V (vs. RHE), it requires a large overpotential in practice because OER transfers 4 electrons to form oxygen-oxygen bonding, being kinetically unfavorable [12–14]. As a result, the role of the OER electrocatalysts became highly important for efficient water electrolysis [11,15]. Exploring transition metals, such as Ni, Co, Fe, Ti, and W, as alternatives to noble metal oxides such as IrO$_2$ or RuO$_2$, has been of particular interest [16–21]. Among them, Ni-based metal oxides like NiFe-layered double hydroxides (LDHs) have been demonstrated as active and cost-effective OER catalysts in alkaline electrolytes, as summarized in Table S1 [22–30]. Bell group revealed that the optimal Ni:Fe ratio of NiFeOOH is around 4:1 in the alkaline OER, suggesting that Fe sites on the edge of NiOOH show a lower overpotential in the OER than the Fe sites located

in the NiFe-LDH framework proven by DFT calculations [31]. Boettcher group reported that a Ni(OH)$_2$ catalyst shows higher activity in the OER in the presence of only 1.0 ppm of Fe in the electrolyte [32].

Despite the cost-effective performance of the NiFe-LDHs in the OER, metal dissolution into the electrolyte can occur during OER, leading to the deactivation of the catalysts [33,34]. Given that renewable energy sources are intermittent in nature, the durable performance of the electrocatalysts under potential fluctuations has become a critical requirement. To resolve the degradation issue, efforts have been made to keep the active sites bound during the working conditions. For example, Najafpour and coworkers investigated the effect of K$_2$FeO$_4$ as soluble Fe additives in alkaline electrolytes on hierarchical Ni(OH)$_2$/Ni catalysts, and observed significantly increased OER performances [35]. Mullins et al. compared the electrocatalytic activity of anodized Ni foam between unpurified KOH and purified KOH, and demonstrated the high performance of the Ni catalyst with anodic treatments [36]. Although Fe impurities and the hierarchical structure of Ni(OH)$_2$/Ni were found beneficial in enhancing the catalytic activity in alkaline OER, details on identifying the effect of Fe on the active site and active phase of Ni-Fe electrocatalysts are still lacking [37–39].

In this study, Fe-doping on electrodeposited Ni(OH)$_2$ and

---

hierarchical Ni(OH)$_2$/Ni were employed, and compared the activity and stability in the OER with NiFe-LDH. More importantly, their activation and degradation mechanisms under potential fluctuation conditions were explored using in situ XANES analysis, which elucidates the superior performance of the hierarchical Fe-doped Ni(OH)$_2$/Ni catalyst over NiFe-LDH with minimal irreversible phase change of Ni(OH)$_2$/NiOOH during potential changes.

## 2. Experimental

### 2.1. Preparation of electrode catalysts

Electrocatalyst samples, including Ni, Ni(OH)$_2$, and NiFe-LDHs, were electrodeposited on a carbon paper (Nara cell tech, density: 0.44 g/cm$^3$, thickness: 0.2±0.01 mm) at − 1.5 mA cm$^{-2}$ for 500 s (Fig. S1), where the respective electrolyte solutions were 0.1 M NiSO$_4$·6 H$_2$O (SAMCHUN, 98.5%), 0.1 M Ni(NO$_3$)$_2$·6 H$_2$O (Alfa Aesar, 99.9985%), and the mixture of 0.1 M of Ni(NO$_3$)$_2$·6 H$_2$O and Fe(NO$_3$)$_3$·9 H$_2$O (SAMCHUN, 98.5%). A two-electrode system with Pt coil and carbon paper (1.5 × 1.0 cm$^2$) as a counter and a working electrode was applied for the electrodeposition. After plating, the electrodes were cleaned with deionized water. After electrodeposition using the Ni and Fe solutions of the Ni: Fe molar ratios 99:1, 97:3, 95:5,90:10, and 80:20, the actual Ni: Fe ratios of electrodeposited catalysts measured by ICP analysis became 99:1, 97:3, 79:21, 19:81, and 16:84, respectively, which were denoted as NiFe-L, -M, -H, − H1, and –H2, respectively. Fe-doping on the electrodeposited Ni(OH)$_2$ (Fe-Ni(OH)$_2$) was conducted with 20 ppm Fe (NO$_3$)$_3$·9 H$_2$O in 1.0 M KOH under 20 cyclic voltammetry (CV) cycles in a potential range of 0–0.9 V (vs. Hg/HgO). In the case of anodized Ni (ANi), the anodic pretreatment proceeded for the electrodeposited Ni at 3.0 V in purified 1.0 M KOH for 1.0 h. Fe-doping for Fe-ANi followed the same method as Fe-Ni(OH)$_2$.

### 2.2. Electrochemical performance

An alkaline solution of 1.0 M KOH (SAMCHUN, 95.0%) was purified with Ni(OH)$_2$, as also introduced in the Boettcher group [32]. High purity Ni(NO$_3$)$_2$·6 H$_2$O (Alfa Aesar, 99.9985%) of 2.0 g was diluted with 5.0 ml deionized water, which was combined with 25 ml of 1.0 M KOH. Ni(OH)$_2$ was deposited downward through centrifugation. Synthesized Ni(OH)$_2$ was centrifugated with deionized water two times and then stirred with 1.0 M KOH for 5 h. After centrifugation, the top layer solution was filtered with a filter paper (Whatman, Grade 1) and used as a purified electrolyte.

Cyclic Voltammetry (CV) and electrochemical impedance spectroscopy (EIS) were measured in purified 1.0 M KOH with a 3-electrode system (ZIVE MP2, WonA Tech Corp.). A Pt coil and Hg/HgO in 1.0 M NaOH were used as counter and reference electrodes, respectively. CVs were conducted in a potential range of 0–0.9 V (vs. Hg/HgO) at room temperature with stirring and were iR-compensated. EIS was measured at 0.7 V (vs. Hg/HgO) in the frequency range from 0.01 Hz to 100 kHz. All electrochemical measurements were conducted in Teflon cells to prevent the effect of Fe in glass cells.

### 2.3. Characterization

X-ray absorption near-edge structure spectroscopy (XANES) was measured at Ni K-edge (8333 eV) and Fe K-edge (7112 eV) on the beamlines 8 C and 10 C of the Pohang Light Source (PLS), which have a flux of 5 × 10$^{12}$ photons s$^{-1}$ at 300 mA and 2.5 GeV. A homemade cell was used in the fluorescence mode for in situ XANES measurements. CV was conducted with a three-electrode system used for electrochemical characterization in the range of 0–0.9 V. The XANES spectra were collected before and after redox behavior. The ex-situ XANES spectra for the references of Ni and Fe foils were also collected. Normalization and background removal of the XANES spectra were carried out using Winxas 3.1 software.

Turnover frequency (TOF) was calculated to determine the intrinsic activity of the electrocatalysts. TOF was calculated at 0.61 V, assuming that the active sites of Ni-Fe electrocatalysts are Ni and Fe, respectively, and the equation is as follows:

$$TOF = \frac{Current\ @\ 0.61V}{Faraday\ constant} \times \frac{1}{moles\ of\ metal\ (Ni\ or\ Fe)} \times \frac{1\ turnover}{4\ electrons}$$

Total moles of active Ni were calculated by integrating redox areas of the anodic (A$_n$) and cathodic peaks (C$_n$) in CV graphs. The redox reversibility according to the CV cycles (R$_n$) was calculated with the ratio of anodic and cathodic peak areas, as suggested in our previous study [40,41]. Inductively coupled plasma atomic emission spectroscopy (ICP-AES, OPTIMA 8300, Perkin-Elmer) was measured to obtain the Ni:Fe molar ratios of electrodes and the amount of Fe content in electrolytes after the OER. The amount of Fe was calculated based on the molar ratio of Ni and Fe from ICP-AES results. The morphology of electrocatalysts before and after OER was examined by a field emission scanning electron microscope (FE-SEM, Hitachi S-4800).

### 2.4. DFT calculations and XANES simulations

The geometry optimization of the model structures was conducted using DMol$^3$ (Material Studio 2019, Accelrys®). The supercell of NiFe-LDH and Fe-Ni(OH)$_2$ was built based on the references of Ni(OH)$_2$ (PDF: 14–117). NiFe-LDH was formed by replacing a Ni atom with a Fe atom, which means there are six Fe and O bonding. In the case of Fe-Ni (OH)$_2$, Fe was doped on the optimized Ni(OH)$_2$ surface. There were three cases of Fe-Ni(OH)$_2$ with different bonding: i) 3(Fe-O)+ 3(Fe-OH), ii) 3(Fe-O)+ 1(Fe-OH), iii) 3(Fe-O)+ 0(Fe-OH). The supercell models were optimized by a density functional theory (DFT) calculation with the DMol$^3$ module. Geometry optimization was carried out with a double-numerical polarization basis set and a cutoff radius of 3.5 Å. It was calculated using the exchange-correlation functional of the local density approximation with the Perdew–Wang as it is widely accepted in calculations involving 2D materials. The convergence criteria for the SCF tolerance were set at 1.0 × 10$^{-6}$ to solve the Kohn-Sham equations. The geometry optimization convergence thresholds for the supercell models were considered as a total energy difference less than 1 × 10$^{-5}$ Ha, a total force difference less than 2 × 10$^{-3}$ Ha/Å, and a maximum displacement of atoms less than 5 × 10$^{-3}$ Å during the optimization. The k-point grid was set according to the 0.07 Å$^{-1}$ k-point separation. The theoretical calculations of Fe K-edge XANES simulations were performed for the geometrically optimized NiFe-LDH and the three cases of Fe-Ni(OH)$_2$ structure using Finite Difference Method Near Edge Structure (FDMNES) with Green function. Calculations were conducted to determine the intensity of white lines in Fe K-edge XANES spectra. Simulations were carried out for clusters with a radius of 5 Å.

## 3. Results and discussion

### 3.1. Degradation behavior of NiFe-LDH electrocatalysts in the OER

Fig. 1 shows the OER performances of electrodeposited Ni(OH)$_2$ and NiFe-LDH samples with the Ni:Fe molar ratios of 99:1, 97:3, and 79:21, denoted as NiFe-L, -M, and –H, respectively. Anodic and cathodic peaks are clearly visible in potential ranges of 0.3–0.5 V (vs. Hg/HgO), which indicates the phase changes between Ni(OH)$_2$ and NiOOH [42,43]. As reported in our previous study, Ni(OH)$_2$ shows a larger anodic peak area in the first CV cycle than in the following cathodic peak, which implies irreversible phase change between NiOOH and Ni(OH)$_2$ due to the lack of conductivity of Ni(OH)$_2$ [40]. The addition of Fe led to the decrease in the OER overpotentials and the redox peak areas (Fig. 1B, C, D), in which the NiFe-H shows the lowest OER overpotential with the smallest redox area among Ni-Fe samples (Fig. 1D). Further increase in the Fe content resulted in a drop in the OER performance, as shown in Figs. S1
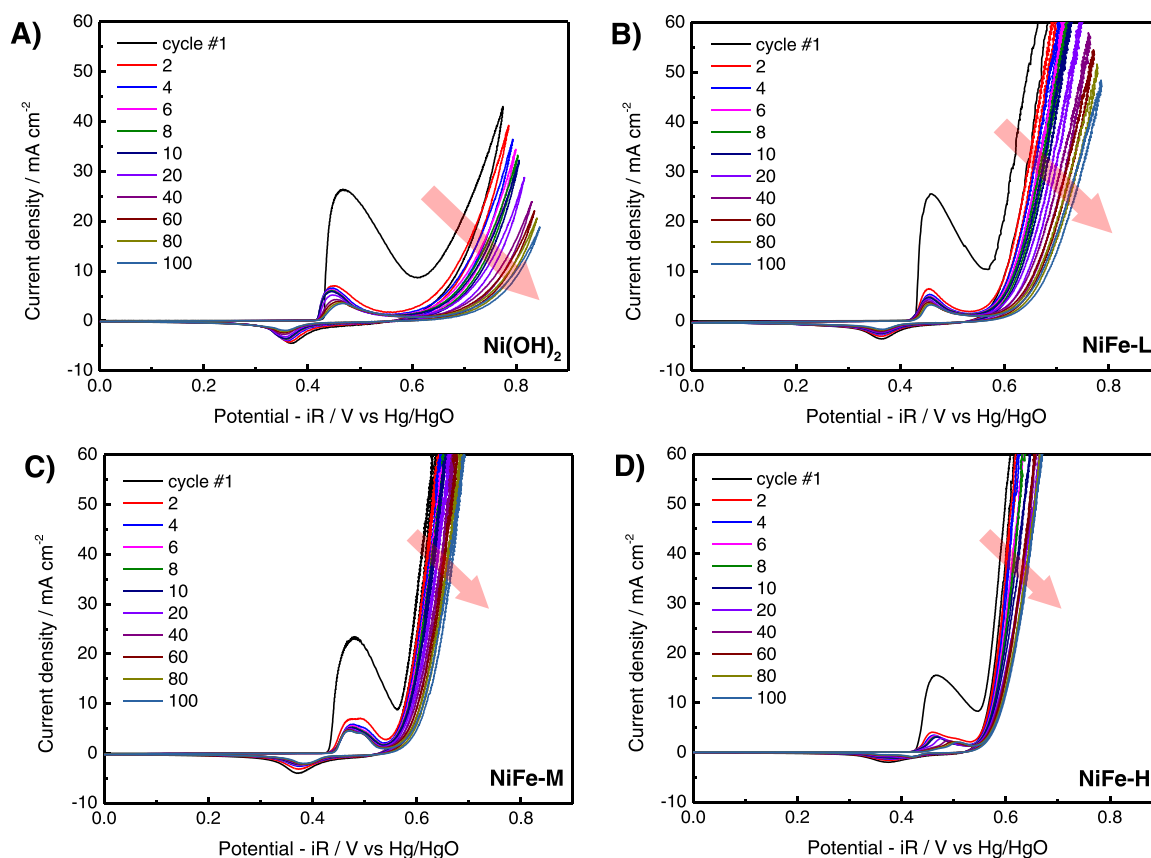
**Fig. 1.** CV graphs of electrodeposited A) Ni(OH)$_2$, and NiFe-LDH with the molar ratio of B) 99:1, C) 97:3, D) 79:21.

and S3. Strasser and coworkers demonstrated that in the case of NiFe-LDH, not all Ni species are oxidized to γ-NiOOH in the anodic potentials while remaining as Ni(OH)$_2$ [28]. Edvinsson et al. also suggested that NiFe-LDH shows a sluggish transition from Ni(OH)$_2$ to NiOOH even at a high overpotential of 200 mV using in situ Raman spectroscopy [16]. Similarly, it can be seen from Fig. 1 that redox potentials of anodic waves of the NiFe-LDH were found to shift from 0.466 to 0.507 V(vs. Hg/HgO). In addition, to figure out the Ni phase in the presence of Fe in the redox potential region, the amount of oxidized Ni was estimated by integrating the first anodic peak area of NiFe-L, -M, -H, which was compared to the moles of electrodeposited Ni measured by elemental analysis. In the case of NiFe-L and -M, the number of moles of Ni calculated by integration of the redox peak of the first CV cycle was similar to the amount of Ni detected by ICP. For example, 6.0 mmol of Ni (OH)$_2$ was oxidized to γ-NiOOH, similarly to the amount of Ni measured by ICP analysis as 5.9 mmol. NiFe-M also shows only 5% of the difference in Ni loadings between the calculated redox peak area (5.8 mmol) and the ICP results (5.6 mmol). The NiFe-H, however, shows a significant difference in the amount of Ni, in which only 1.4 mmol out of 4.2 mmol of Ni was oxidized. These results indicate that the oxidation of Ni was suppressed by the presence of Fe. In addition, more loadings of Fe led to an increase in the overpotential in the OER. For example, NiFe-LDH samples with Ni/Fe ratios of 19:81 (NiFe-H1) and 16:84 (NiFe-H2) exhibited high overpotentials of 260.2 and 328.0 mV at 15 mA cm$^{-2}$, respectively (Fig. S3A, B). The catalytic deactivation was also observed in NiFe-H1 and NiFe-H2, of which overpotentials were 0.619 and 0.679, respectively, after 100 CV cycles (Fig. S3C). These results are related to the increased charge transfer resistances, as evident by the large diameter of Nyquist semicircles for NiFe-H1 and NiFe-H2 (Fig. S3D). It can be inferred that the addition of excess Fe could lower the conductivity and cause a decrease in the catalytic activities in the OER. Similar results were reported by Bell et al., suggesting that the

redox of Ni(OH)$_2$/NiOOH became restricted with the addition of Fe, and 25% of Fe in NiFe-LDH showed the highest performance in the OER [31]. In addition, they suggested that too much Fe loading causes the formation of inactive γ-FeOOH and isolates the active γ-NiOOH.

Fig. 2 shows the profiles of overpotentials at 15 mA cm$^{-2}$ during 100 CV cycles and EIS results before and after the CV cycles. It was observed that the overpotentials at the 100$^{th}$ CV cycle were increased by 104.8, 46.2, and 40.3 mV in NiFe-L, -M, and -H, respectively, compared to those at the first CV cycle. The diameters of Nyquist semicircles of NiFe-L, M, and H were found much smaller than that of Ni(OH)$_2$, particularly with that of NiFe-H being the lowest at 0.52 Ω cm$^2$. After 100 CV cycles, the Nyquist semicircle areas increased in all NiFe-LDH samples from 1.03, 0.84, 0.52 Ω cm$^2$ to 1.70, 1.16, 0.71 Ω cm$^2$ for NiFe-L, M, H, respectively (Fig. 2C, Table 1). These results suggest that although the co-electrodeposition of Ni and Fe improves the OER performances, the degradation of the NiFe-LDH electrodes is still problematic upon the potential fluctuations.

To investigate the activation and degradation mechanism of NiFe-LDH, in situ XANES spectra were collected for NiFe-H during CV cycles, as shown in Fig. 3. The oxidation state of absorbing elements can be characterized by the energy position of the white lines caused by 1 s to 4p transition. The XANES spectra of Ni(OH)$_2$ and γ-NiOOH exhibit sharp white lines centered at 8351.8 and 8354.9 eV, respectively. γ-NiOOH has a white line shifted about 3 eV to the right of Ni(OH)$_2$, which is consistent with the recent study by the Nocera group [42]. They reported that the XANES spectra of Ni(OH)$_2$, β-NiOOH, and γ-NiOOH show E$_o$ positions at 8342.4, 8343.7, and 8345.0 eV, respectively, leading to the difference between the white line positions of 1.3 eV each. The Ni K-edge XANES spectrum of NiFe-H gives the white line centered at 8351.8 eV at 0.4 V (state I), which is well matched with Ni(OH)$_2$. After the anodic oxidation (state II), the white line has shifted to higher energy centered at 8354.8 eV, indicating the phase transformation of Ni from Ni
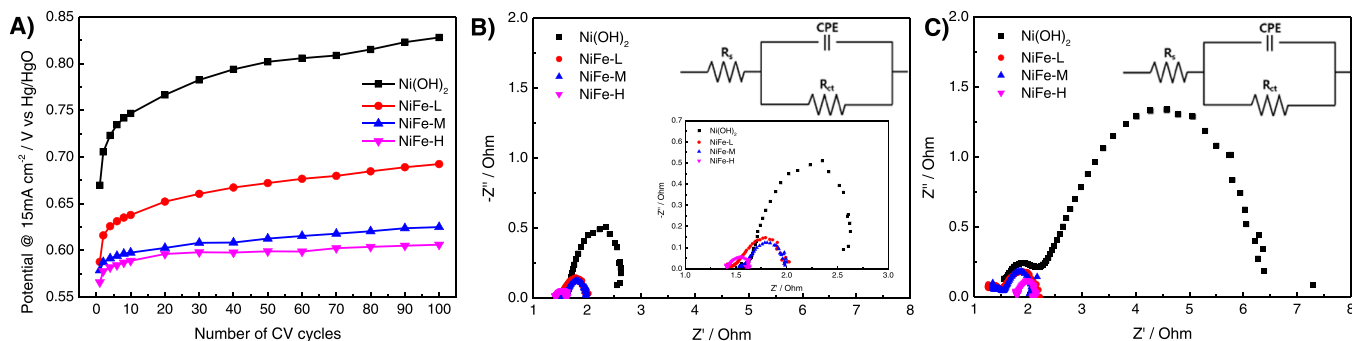
**Fig. 2.** A) Potential changes with the number of CV cycles and EIS results of electrodeposited Ni(OH)$_2$ and NiFe-LDH B) before CV, C) after 100 CV cycles.

**Table 1**
Summary of electrodeposited electrocatalysts and performances in the OER.

| Sample | η @ 15 mA cm$^{-2}$ / mV | | ICP results / Ni:Fe (in mol%) | | TOF$_{Ni}$ @ 0.61 V / s$^{-1}$ | | TOF$_{Fe}$ @ 0.61 V / s$^{-1}$ | | R$_{ct}$/Ωcm$^2$ | |
|---|---|---|---|---|---|---|---|---|---|---|
| | 1$^{st}$ cycle | 100$^{th}$ cycle | 1$^{st}$ cycle | 100$^{th}$ cycle | 1$^{st}$ cycle | 100$^{th}$ cycle | 1$^{st}$ cycle | 100$^{th}$ cycle | Before CV | After CV |
| Ni | 498.6 | – | – | – | 0.004 | 0.003 | – | – | 9.01 | 11.32 |
| ANi | 479.9 | 512.0 | – | – | 0.016 | 0.014 | – | – | 2.12 | 4.83 |
| Ni(OH)$_2$ | 363.7 | 522.0 | – | – | 0.007 | 0.004 | – | – | 2.02 | 6.55 |
| NiFe-L | 281.7 | 386.5 | 99:1 | 99:1 | 0.026 | 0.012 | 3.014 | 0.834 | 1.03 | 1.70 |
| NiFe-M | 272.7 | 318.9 | 97:3 | 98:2 | 0.041 | 0.043 | 1.164 | 1.545 | 0.84 | 1.16 |
| NiFe-H | 259.8 | 300.1 | 79:21 | 81:19 | 0.111 | 0.262 | 0.355 | 0.825 | 0.52 | 0.71 |
| Fe-Ni(OH)$_2$ | 308.1 | 277.5 | – | 88:12 | 0.010 | 0.125 | – | 0.944 | – | 0.97 |
| Fe-ANi | 285.1 | 270.5 | – | 94:6 | 0.312 | 0.205 | – | 0.966 | – | 0.58 |
| Fe(OH)$_3$ | – | – | – | – | – | – | 0.0001 | – | 134.05 | |
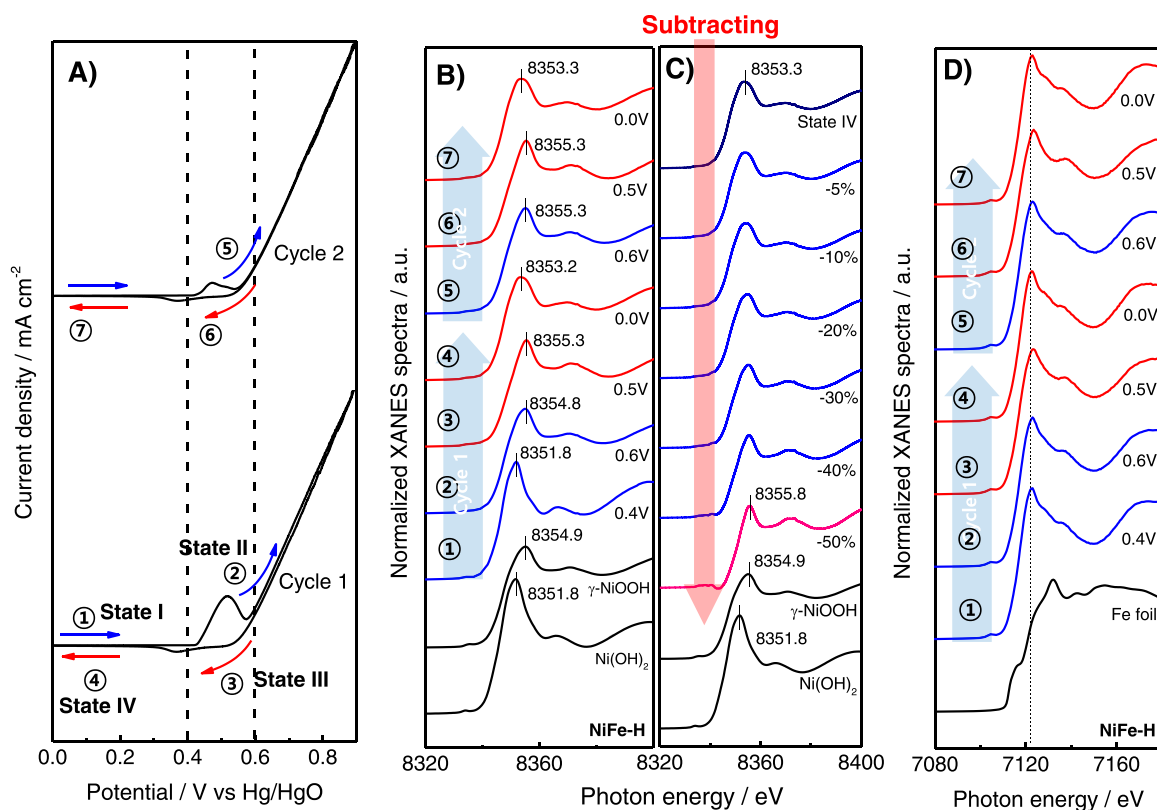


**Fig. 3.** In situ XANES spectra of NiFe-H; A) CV graphs, B) Ni K-edge spectra, C) XANES subtraction: χ[State IV]-χ[Ni(OH)$_2$], D) Fe K-edge spectra.

(OH)$_2$ to γ-NiOOH. These results show that the Ni$^{2+}$ is oxidized to Ni$^{3.6+}$ above the OER onset potential for NiFe-H to be active in the OER. In the following cathodic potential region, a negative shift of the white line position from 8355.3 to 8353.2 eV was observed (state IV), which is related to the fact that the phase of γ-NiOOH is not fully reduced to Ni(OH)$_2$ in the cathodic potential region, as also confirmed in our previous study [40]. The spectrum shifted to the right after the second CV cycle, the same as the first CV cycle (8353.3 eV). Considering that the XANES

spectrum is a combined contribution of the individual spectrum between the absorbing atom and the neighboring scatters, the XANES spectrum obtained at state IV can include the integrated feature of the NiOOH and Ni(OH)$_2$ phases. In order to separate the mixed Ni phases during the CV cycles, the XANES spectrum of state IV was subtracted by that of a reference XANES spectrum for Ni(OH)$_2$, as shown in Fig. 3C. It can be observed that with the subtraction of Ni(OH)$_2$ phase, the spectrum shifted with a white line centered at 8355.8 eV, corresponding to the XANES spectrum of γ-NiOOH. On the other hand, the Fe K-edge XANES spectra for the NiFe-H have shown almost the same feature with the white line centered at 7123.0 eV regardless of potential changes (Fig. 3D). This is in line with the Fe K-edge XANES spectra of Ni$_{0.75}$Fe$_{0.25}$OOH studied by Friebel et al., in which the phase of γ-FeOOH was identified. These results thus demonstrated that although the Fe phase in NiFe-LDH remains still as Fe$^{3+}$ with potential changes, the irreversible phase change between Ni(OH)$_2$ and γ-NiOOH is still observed for NiFe-LDH during potential fluctuations.

It has been reported that Fe dissolution is one of the main reasons for the degradation of NiFe-LDH electrodes [33,34]. For example, the Chen group studied various NiFe-based electrocatalysts for the OER, and suggested that Fe was dissolved after the OER in NiFe-LDH [33]. Peng et al. also reported that metal dissolution under high OER potentials could cause the degradation of mixed metal hydroxides [34]. In order to examine the extent of Fe dissolution of NiFe-LDH samples under potential fluctuations, elemental analysis was conducted for the NiFe-LDH samples before and after the CV cycles, as presented in Fig. S2. It can be seen that as the amount of Fe increases, the molar ratio of Fe/Ni rapidly decreases after CV cycles. The higher content of Fe in NiFe-LDH, the more Fe dissolution was observed. For example, the Fe/Ni ratio of the NiFe-H1 and NiFe-H2 drastically decreased from 1.67 and 5.4–1.26 and 0.39, respectively. These results suggest that Fe dissolution could be another critical factor inducing the deactivation of NiFe-LDH electrocatalysts during potential fluctuations.

### 3.2. The effect of Fe-doping on Ni(OH)$_2$ electrocatalysts for OER

It has been known that the presence of a small amount of Fe in electrolytes affects OER performances [27,35,36,44]. For example, the

Boettcher group studied Fe incorporation onto NiOOH electrodes by Fe impurity in the electrolytes and confirmed a dramatic increase in the OER performance due to the improvement of the electronic conductivity of the electrodes [26]. In addition, the Najafpour group studied the effect of soluble Fe impurity (K$_2$FeO$_4$) on anodized Ni foams in the OER and suggested that Fe$^{4+}$ is reduced to Fe$^{3+}$ and adsorbed to the Ni electrode, which leads to a higher OER activity [35]. However, verifying the active phase and sites of Fe-adsorbed Ni is still necessary.

Fig. 4 shows the electrochemical performance of Fe-doped Ni(OH)$_2$, denoted as Fe-Ni(OH)$_2$, for the OER. To prepare the Fe-Ni(OH)$_2$ sample, 20 ppm of Fe(NO$_3$)$_3$ was dissolved in 1.0 M KOH. Differently from the cases for Ni(OH)$_2$ or NiFe-H that suffer from deactivation during CV cycles, the current density for Fe-Ni(OH) in the OER region kept rising with the CV cycles (Fig. 4A). It is obvious that the overpotential of the OER for Fe-Ni(OH)$_2$ became lowered in the early stage of CV cycles, and stabilized after 20 cycles (Table 1, Fig. 4B). It can be noted that Fe-Ni(OH)$_2$ has shown low and stable overpotentials compared to NiFe-H. The diameter of the Nyquist semicircle of Fe-Ni(OH)$_2$ significantly decreased, indicating high conductivity by doping Fe on Ni(OH)$_2$ (Fig. 4C, Table 1). Differently from the degradation behavior of Ni(OH)$_2$ electrocatalysts with the poor redox phase reversibility between Ni(OH)$_2$ and NiOOH, the phase reversibility was substantially improved by Fe doping (Fig. 4D, E, F). In the case of Ni(OH)$_2$ and NiFe-H, the phase reversibility in the first CV cycle (R$_1$) calculated by the ratio of the anodic charge to the cathodic charge was 0.269 and 0.297, respectively. On the contrary, R$_1$ of Fe-Ni(OH)$_2$ increased to 0.606, which is more than twice as much as Ni(OH)$_2$ and NiFe-LDH. This high value of R$_1$ was mainly due to the enhanced cathodic charge, which contributed to the increased phase stability of Fe-Ni(OH)$_2$. In addition, the amount of anodic charge of Fe-Ni(OH)$_2$ decreased rapidly according to the CV cycles, but the amount of cathodic charge was always higher than Ni(OH)$_2$ and NiFe-H. These changes resulted in Fe-Ni(OH)$_2$ having an R$_n$ value greater than 1, which suggests that Fe doping not only prevents the isolation of γ-NiOOH but also helps the reduction of γ-NiOOH. Vallejo et al. also suggested that active sites of NiFe-LDH are Fe [26]. They obtained the overpotentials of NiMOOH (M=Mn, Fe, Co, Cu, Zn, Cr) using DFT calculations and suggested that the M site is the active site in the OER. The Carter group demonstrated that Fe makes the discharge
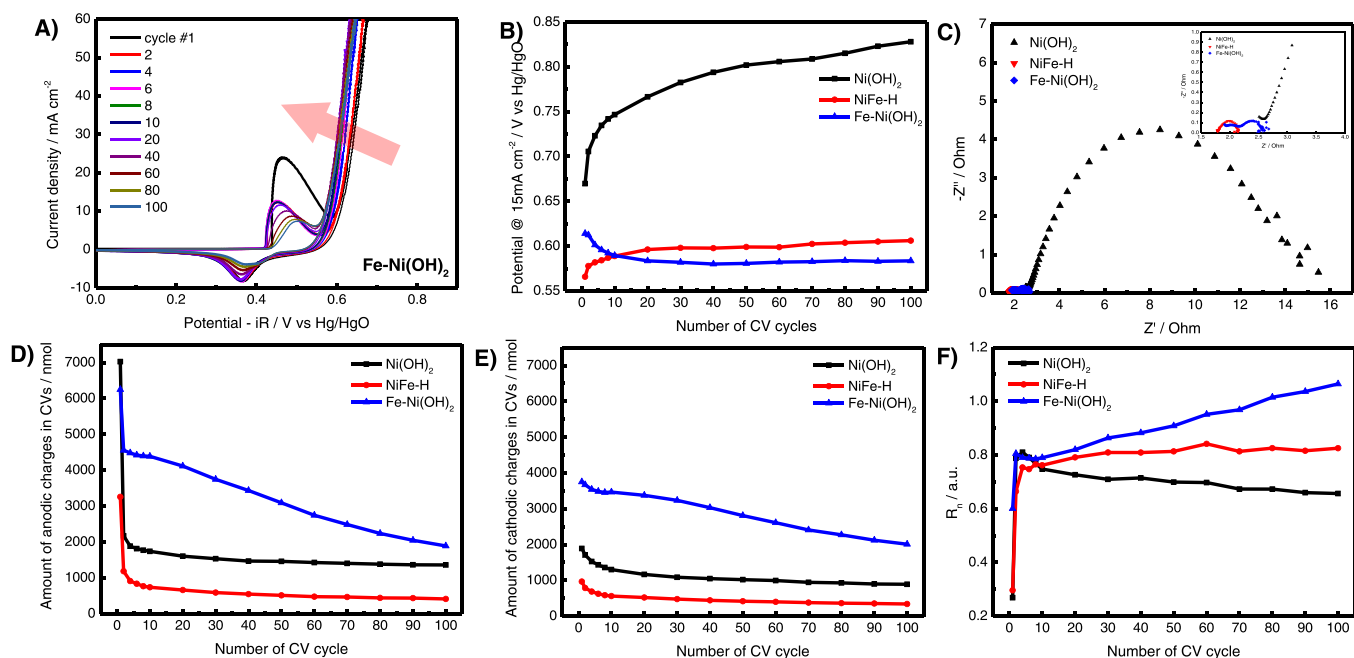


**Fig. 4.** Effect of Fe in electrolytes with Ni(OH)$_2$: A) CV graph of Fe-Ni(OH)$_2$, B) Potentials at 15 mA cm$^{-2}$ with 100 CV cycles, C) Nyquist semicircles of Fe-Ni(OH)$_2$, D) Amount of Ni calculated by anodic peak areas, E) Amount of Ni calculated by cathodic peak areas, F) Reversibility (R$_n$) with the number of CV cycles.

of $Ni^{3+}$ to $Ni^{2+}$ favorable in the OER by DFT calculations [45]. These are supportive of our results that Fe-Ni(OH)$_2$ has shown better activity and stability in the OER.

Fig. 5 presents the Ni K-edge XANES spectra for Fe-Ni(OH)$_2$, which were collected after the first anodic wave, i.e., OER condition at 0.7 V (state II) and after the following cathodic wave at 0 V (state IV). It can be seen that the XANES spectrum of Fe-Ni(OH)$_2$ at 0.7 V shows the white line centered at 8354.9 eV, which indicates that $Ni^{2+}$ is oxidized to $Ni^{3.6+}$ in the OER conditions. In the following reductive potential (state IV), although the spectrum is not fully recovered to the original phase of Ni(OH)$_2$, it shifted more to the left than in the case of the NiFe-H. This result indicates that Fe-Ni(OH)$_2$ is more reversible under potential fluctuations than NiFe-H, which is in line with the high reversibility of Fe-Ni(OH)$_2$ in Fig. 4F.

Fig. 6 compares SEM images of Ni(OH)$_2$, NiFe-H, and Fe-Ni(OH)$_2$ before and after 100 CV cycles. It can be seen that Ni(OH)$_2$ is homogeneously deposited on the carbon paper right after the electrodeposition (Fig. 5A). After the 100 CV cycles, however, a large part of Ni(OH)$_2$ was agglomerated and degraded (Fig. 5B). In the case of NiFe-H, the non-uniform distribution of Ni and Fe was observed, and the layered structure of Ni was hardly observed due to the aggregation of FeOOH
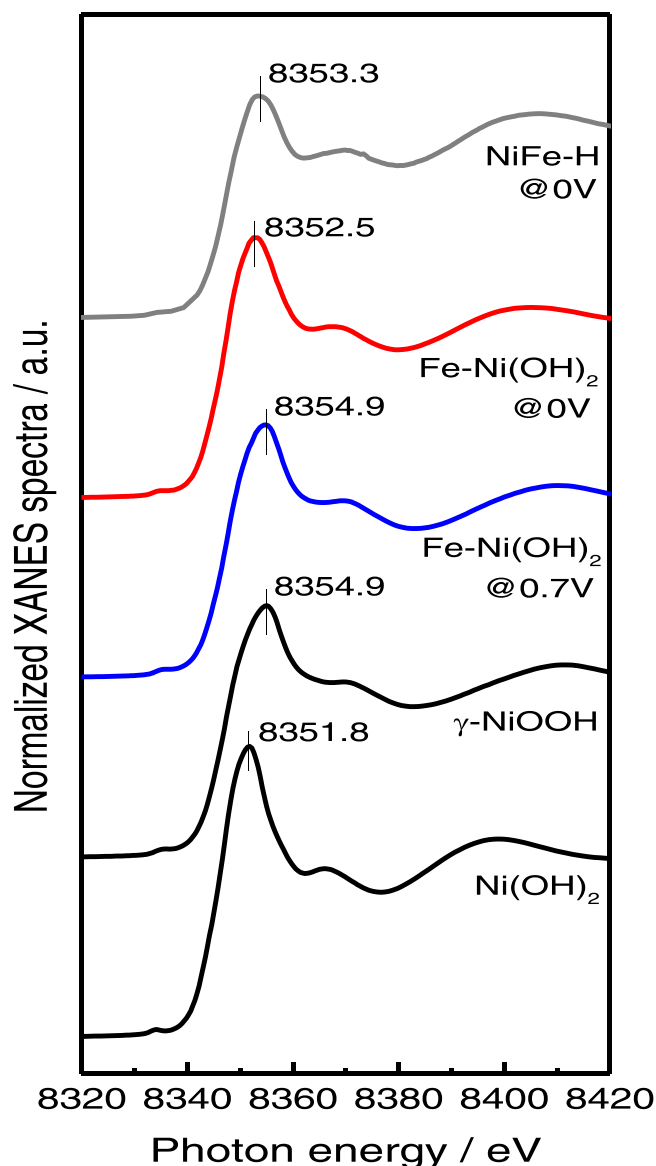
(Fig. 6C) [46]. On the contrary, Fe-Ni(OH)$_2$ shows the homogeneous and well-adhered structure of Ni(OH)$_2$, and the layered structure of Ni(OH)$_2$ was well maintained after the 100 CV cycles (Fig. 5D). These results are in line with the high stability investigated by CV and XANES measurement that electrodeposited Ni in Fe-Ni(OH)$_2$ shows higher structural stability than Ni(OH)$_2$ and NiFe-H due to its high redox reversibility with CV cycles.

### 3.3. High activity and stability of Fe-doped anodized Ni in the OER

Although Ni(OH)$_2$/NiOOH catalyst system has the advantage of a layered structure that allows all Ni sites to be accessible and active in the OER, the low conductivity of NiOOH at a low potential range causes degradation, leading to the irreversible redox phase changes and phase isolations. Najafpour group obtained Ni(OH)$_2$ phase on the surface of Ni by applying anodic potential treatment, and the hierarchical structure of Ni(OH)$_2$/Ni has been reported to show high activity in the OER due to its superior conductivity over Ni(OH)$_2$/NiOOH [35].

Herein, a hierarchical Ni(OH)$_2$/Ni sample was also prepared by applying the anodic potential of 3 V to the electrodeposited Ni, denoted as ANi. The electrochemical performance during CV cycles of the parent Ni and ANi samples is presented in Fig. 7 and S4. The Ni(OH)$_2$/NiOOH redox peak areas were observed to be more prominent in ANi than in Ni, indicating that Ni(OH)$_2$ phase is formed on Ni by anodic potential treatment. The overpotentials in the OER were also lower for ANi (479.9 mV) than for Ni (498.6 mV). Still, both samples experienced degradation with CV cycles (Table 1, Fig. 7A). The diameter of the Nyquist semicircle of Ni largely decreased by anodization with a similar charge transfer resistance (Rct) to Ni(OH)$_2$ as 2.12 $\Omega$ cm$^2$. The effect of Fe-doping on the ANi for the OER performance was also investigated as given in Fig. 7 and S4. It is noted that the OER performance of the Fe-ANi is remarkably increased with a small redox peak area. These results indicate that Ni(OH)$_2$ on the Ni surface is not likely oxidized to $\gamma$-NiOOH. In the first CV cycle, Fe-ANi shows a lower OER overpotential of 285.1 mV at 15 mA cm$^{-2}$ than Fe-Ni(OH)$_2$ (Fig. 7A, B). After the 100 CV cycles, Fe-ANi still maintained the lowest overpotentials at 270.5 mV, which is much lower than NiFe-H (300.1 mV) and Fe-Ni (OH)$_2$ (277.5 mV). The charge transfer resistance of Fe-ANi after 100 CV cycles was found to be substantially low at 0.58 $\Omega$ cm$^2$, compared to those of Fe-Ni(OH)$_2$ and NiFe-H (Fig. 7D). These results suggest that the enhanced conductivity and phase stability of Fe-ANi contributed to the outperformance in the OER.

In situ Ni and Fe K-edge XANES analysis during CV cycles was conducted to identify the active phase of Fe-ANi, as presented in Fig. 8. In Ni K-edge XANES, the phase of Ni was dominant in all spectra with a slight development of white line intensity at the similar position to Ni(OH)$_2$, implying the formation of Ni(OH)$_2$ phase on the surface of Ni. Moreover, there was no significant shift in the white line position during the CV cycles. In the case of Fe K-edge XANES, all the spectra remained still regardless of the potential changes with the white line position centered at 7123.0 eV.

In order to identify the active phases in the potential fluctuations, the XANES spectra collected during the CV cycles were subtracted by that of a reference XANES spectrum for Ni, as shown in Fig. 9A-D. It can be observed that with the subtraction of the Ni phase, the spectrum shifted with a white line centered at 8351.5 $\pm$ 1.0 eV, corresponding to the XANES spectrum of Ni(OH)$_2$, which means that the hierarchical structure of Ni(OH)$_2$/Ni was well formed by anodization (Fig. 9A). What is surprising is that the white line position of Ni(OH)$_2$ did not shift to the right with anodic potentials. The subtracted Fe-ANi spectrum at state II shows the white line position centered at 8352.5 eV, indicating that most of Ni(OH)$_2$ was maintained as $Ni^{2+}$ (Fig. 9B). In the 2nd CV cycle, the white line position was still held at 8325.5 eV at 0.6 V. After the OER, the white line shifted by 1 eV to the positive direction and fully returned to 8352.0 eV with the cathodic potential. The 3rd cycle showed the same trend as the 2nd cycle. These results suggest that the phase of Ni
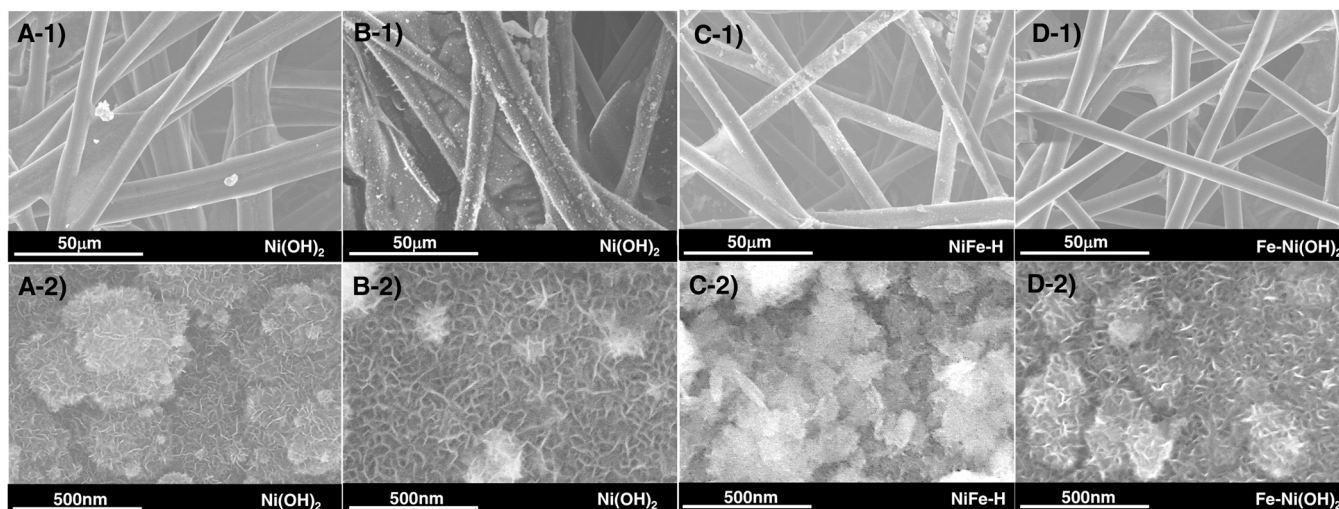


**Fig. 5.** Ni K-edge XANES spectra of Fe-Ni(OH)$_2$.

**Fig. 6.** SEM images of A) Fresh Ni(OH)$_2$, B) 100 CV cycled Ni(OH)$_2$, B) 100 CV cycled NiFe-H, C) 100 CV cycled Fe-Ni(OH)$_2$.



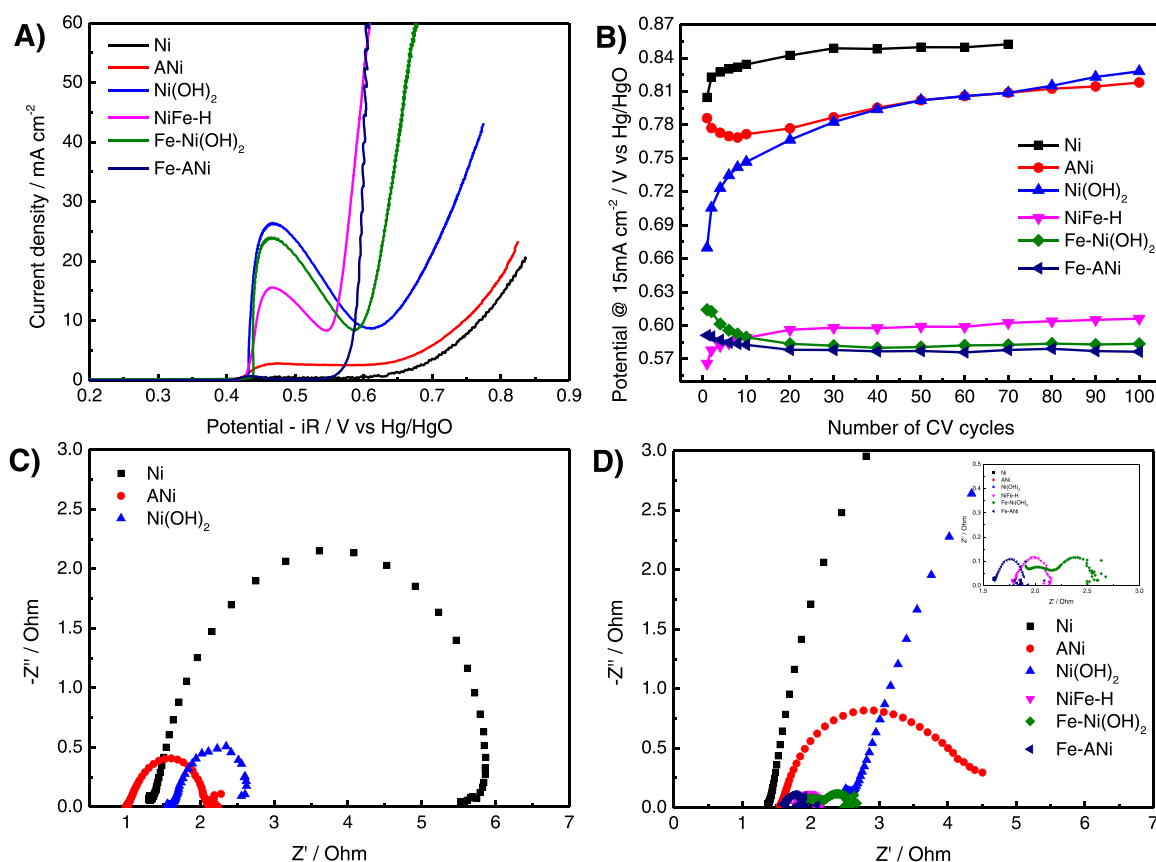**Fig. 7.** Effect of anodic pretreatment and Fe doping: A) LSV curves of Ni-based electrocatalysts, B) Potentials at 15 mA cm$^{-2}$ in 100 CV cycles, EIS graphs of B) before CV, C) after CV.

is not significantly changed with the potentials, unlike the case of Ni(OH)$_2$ and NiFe-H. This is in line with the stable redox behavior of Fe-ANi (Fig. 7B), which suggests that Fe doping effectively suppresses the phase change of Ni$^{2+}$ and leads to highly active and stable performance in the OER.

Although the Fe XANES spectra between NiFe-H and Fe-ANi appeared similar, it can be noted that their white line intensities were observed to be quite different, with the former being stronger, as presented in Figs. 3D and 8C, respectively. To clarify the difference between

the local structures of the Fe species in NiFe-LDH and Fe-ANi, the Fe K-edge XANES simulations were conducted for optimized model structures obtained by DFT calculations, as given in Fig. 10. The model structure of NiFe-LDH was optimized with Fe species located within the frameworks of Ni(OH)$_2$ slab, having 6 Fe-O coordinations around Fe. Given that Fe-doping occurs on the surface of Ni(OH)$_2$ phase for Fe-ANi, three possible cases of Fe coordination on the surface of Ni(OH)$_2$ slab were assumed to simulate Fe-doped Ni(OH)$_2$ structure: 1) 3(Fe-O)+ 3(Fe-OH), 2) 3(Fe-O)+ 1(Fe-OH), and 3) 3(Fe-O)+ 0(Fe-OH). It can be seen that the more
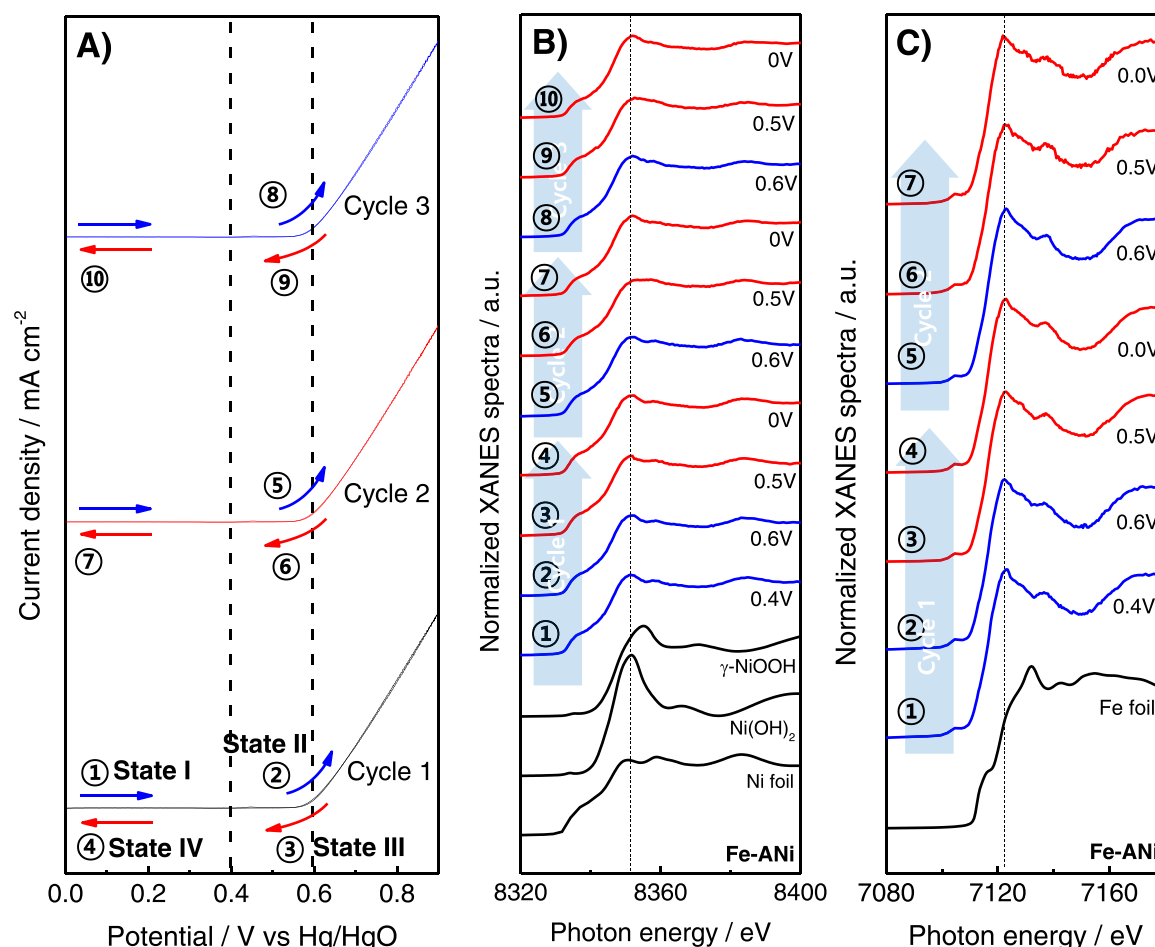
**Fig. 8.** In situ XANES spectra of Fe-ANi: A) CV graphs, B) Ni K-edge spectra, C) Fe K-edge spectra.

Fe species are bound to the O of $Ni(OH)_2$ framework, like in the case of NiFe-LDH of 6 Fe-O coordinations, the stronger the white line intensity of the simulated Fe K-edge XANES spectrum becomes. On the contrary, if the Fe species are less bound by the O of $Ni(OH)_2$ framework with more exposure, like Fe-ANi of 3 Fe-O coordinations, the white line intensity becomes weaker. These results are in accordance with the XANES results obtained for NiFe-H and Fe-ANi, in which the former shows the stronger intensity of the white line (Figs. 3D and 8C). Likewise, it can be conceivable that Fe is doped on the surface of $Ni(OH)_2$ of the hierarchical structure of ANi, and it shows the highest activity and stability in the OER. Bell et al. suggested that Fe on top of the Ni surface acts as an active site and exhibits lower overpotentials than Fe in the NiFe-LDH structure in the OER using DFT calculations.

To determine the intrinsic activities of the catalyst samples, the turnover-frequency (TOF) was obtained on the basis of the mole number of Ni ($TOF_{Ni}$) and Fe ($TOF_{Fe}$) at 0.61 V (vs. Hg/HgO), as listed in Table 1. The NiFe-L, M, and H show higher values of 0.026, 0.041, and 0.111 $s^{-1}$, respectively, than $Ni(OH)_2$ (0.007 $s^{-1}$) and $Fe(OH)_3$ (0.0001 $s^{-1}$), indicating the synergetic effect between Ni and Fe on the OER as also observed in previous studies [47,48]. In the case of Fe-$Ni(OH)_2$, $TOF_{Ni}$ at the 100th CV cycle shows a higher value of 0.125 $s^{-1}$ than that at the 1st CV cycle of 0.01 $s^{-1}$, which suggests that the intrinsic activity of $Ni(OH)_2$ was enhanced by Fe-doping during the CV cycles. Moreover, it is noted that the $TOF_{Fe}$ of Fe-$Ni(OH)_2$ shows a higher value of 0.944 $s^{-1}$ than that of NiFe-H of 0.825 $s^{-1}$ at the 100th CV cycle, which is in line with the results that Fe-$Ni(OH)_2$ shows lower overpotentials than NiFe-H after 100 CV cycles. Fe-ANi showed a much lower overpotential than Fe-$Ni(OH)_2$ and NiFe-H and exhibited the highest $TOF_{Fe}$ of 0.966 $s^{-1}$. These results suggest that Fe sites on the surface of $Ni(OH)_2$ are active sites for

the OER.

Since Fe dissolution is problematic in NiFe-LDH under potential swings [33,34], it is necessary to confirm the stability of Fe-doped Ni$(OH)_2$ and ANi under potential fluctuations. The Fe-$Ni(OH)_2$ and Fe-ANi samples after the 20th CV cycle were moved to Fe-free KOH solutions. In the subsequent CV cycles (Fig. S5), the OER overpotentials for Fe-Ni$(OH)_2$ at 15 mA $cm^{-2}$ were found to increase by 21.8% during the CV cycles in purified KOH. These results indicate that the degradation of Fe-$Ni(OH)_2$ is attributed to the irreversible phase change Ni$(OH)_2$/NiOOH during the potential fluctuations, facilitating the loss of Fe. Nevertheless, Fe-ANi shows higher stability than Fe-$Ni(OH)_2$, with a slight increase of overpotential by 5.9% during 100 CV cycles, which suggests that the Fe-doping onto the hierarchical $Ni(OH)_2$/Ni structure allows for suppression of phase transformation of $Ni(OH)_2$/NiOOH during the potential fluctuations, contributing highly active and stable OER performance even under potential fluctuation.

## 4. Conclusions

The potential-dependent nature of evenly Fe-doped anodic pretreated Ni electrocatalysts was investigated to demonstrate activation and degradation mechanism in alkaline OER. The case of conventional NiFe-LDH, obtained by the co-electrodeposition, presents lower overpotential in OER than $Ni(OH)_2$, but still shows 15% degradation during 100 CV cycles. The in situ XANES analysis confirmed that γ-NiOOH was still isolated during CV cycles, as seen in $Ni(OH)_2$. In contrast, Fe-doped to $Ni(OH)_2$ obtained by adding 20 ppm of Fe to the electrolytes (Fe-Ni$(OH)_2$) led to a lower overpotential and showed high activity and stability during 100 CV cycles. To realize a better conductivity
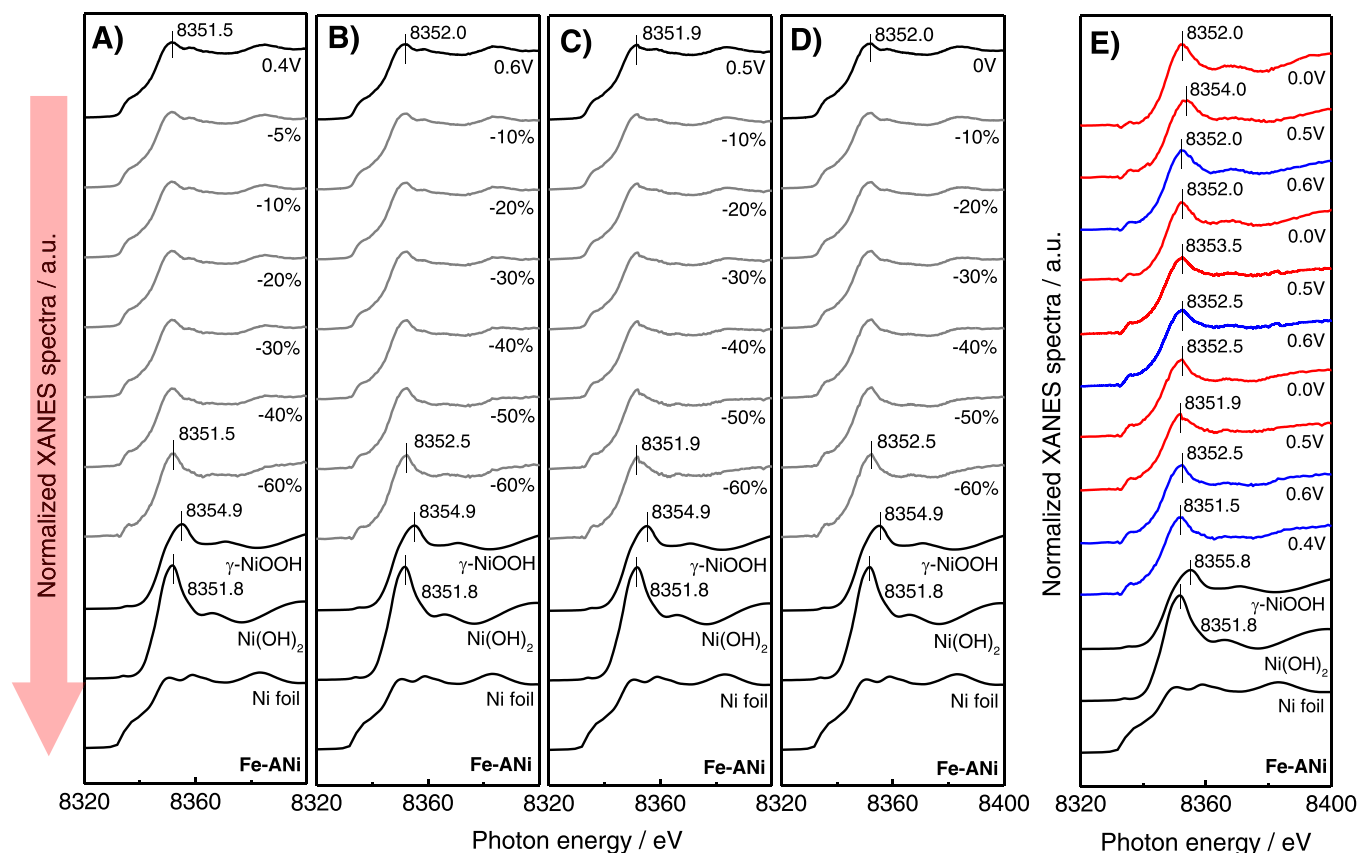
**Fig. 9.** XANES subtraction of Fe-ANi: A) $\chi$[State I]-$\chi$[Ni foil], B) $\chi$[State II]-$\chi$[Ni foil], C) $\chi$[State III]-$\chi$[Ni foil], D) $\chi$[State IV]-$\chi$[Ni foil], E) subtracted XANES spectra.
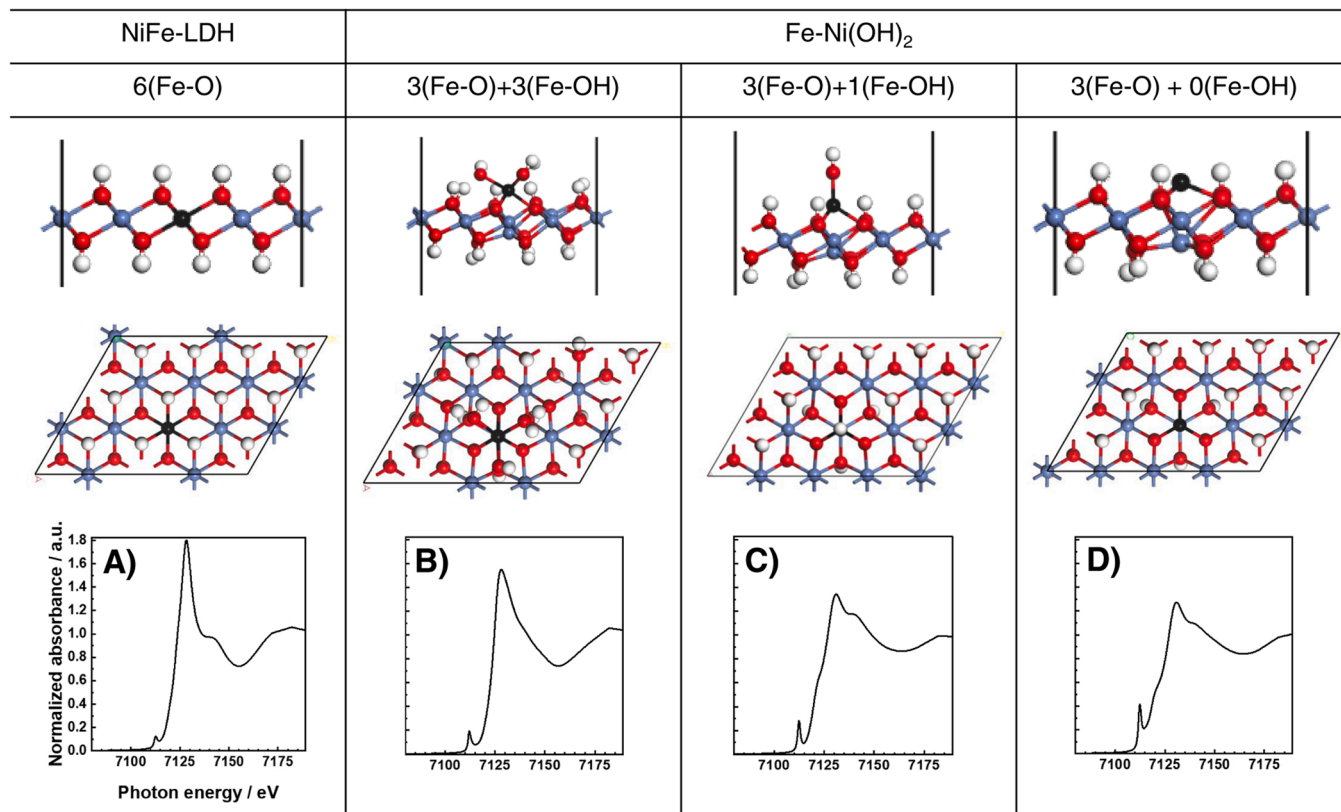


**Fig. 10.** DFT and XANES simulations of NiFe-LDH and Fe-Ni(OH)$_2$.

environment, anodic oxidation of Ni was applied at 3 V to obtain Ni $(OH)_2$ on the surface of the Ni phase (ANi). It shows even better activity and stability than NiFe-LDH. The Ni phase of Fe-ANi is maintained as $Ni^{2+}$ regardless of potential changes. Fe-ANi also shows a lower white line intensity and a higher pre-edge intensity in the Fe K-edge XANES, which proves the adsorption of Fe on the surface of Ni. Overall, these findings provide important insight that a highly active and durable OER catalyst can be obtained by anodic pretreatments of Ni foam followed by Fe-doping.

## CRediT authorship contribution statement

Sang-Yeon Lee: Data curation and Writing – original draft. **Hyun-Jung Oh:** Formal analysis. **MinJoong Kim:** Conceptualization. **Hyun-Seok Cho:** Methodology, Funding acquisition. **Yong-Kul Lee:** supervision, Writing – review & editing.

## Declaration of Competing Interest

The authors declare that they have no known competing financial interests or personal relationships that could have appeared to influence the work reported in this paper.

## Data Availability

Data will be made available on request.

## Acknowledgment

## Appendix A. Supporting information

Supplementary data associated with this article can be found in the online version at doi:10.1016/j.apcatb.2022.122269.

## References

[1] M.V. Ramos-Garcés, J. Sanchez, D.E. Del Toro-Pedrosa, I.B. Alvarez, Y. Wu, E. Valle, D. Villagrán, T.F. Jaramillo, J.L. Colón, Transition metal-modified exfoliated zirconium phosphate as an electrocatalyst for the oxygen evolution reaction, ACS Appl. Energy Mater. 2 (2019) 3561–3567, https://doi.org/10.1021/acsaem.9b00299.
[2] G. Fang, J. Cai, Z. Huang, C. Zhang, One-step electrodeposition of cerium-doped nickel hydroxide nanosheets for effective oxygen generation, RSC Adv. 9 (2019) 17891–17896, https://doi.org/10.1039/c9ra02682g.
[3] B. Lassalle-Kaiser, S. Gul, J. Kern, V.K. Yachandra, J. Yano, In situ/Operando studies of electrocatalysts using hard X-ray spectroscopy, J. Electron Spectros Relat. Phenom. 221 (2017) 18–27, https://doi.org/10.1016/j.elspec.2017.05.001.
[4] B.M. Hunter, W. Hieringer, J.R. Winkler, H.B. Gray, A.M. Müller, Effect of interlayer anions on [NiFe]-LDH nanosheet water oxidation activity, Energy Environ. Sci. 9 (2016) 1734–1743, https://doi.org/10.1039/c6ee00377j.
[5] Z. Cai, X. Bu, P. Wang, J.C. Ho, J. Yang, X. Wang, Recent advances in layered double hydroxide electrocatalysts for the oxygen evolution reaction, J. Mater. Chem. A Mater. 7 (2019) 5069–5089, https://doi.org/10.1039/c8ta11273h.
[6] C.F. Li, T.Y. Shuai, L.R. Zheng, H.B. Tang, J.W. Zhao, G.R. Li, The key role of carboxylate ligands in Ru@Ni-MOFs/NF in promoting water dissociation kinetics for effective hydrogen evolution in alkaline media, Chem. Eng. J. 451 (2022), https://doi.org/10.1016/j.cej.2022.138618.
[7] T.T.H. Hoang, A.A. Gewirth, High activity oxygen evolution reaction catalysts from additive-controlled electrodeposited Ni and Nife films, ACS Catal. 6 (2016) 1159–1164, https://doi.org/10.1021/acscatal.5b02365.
[8] M. Al Samarai, A.W. Hahn, A. Beheshti Askari, Y.T. Cui, K. Yamazoe, J. Miyawaki, Y. Harada, O. Rüdiger, S. Debeer, Elucidation of structure-activity correlations in a nickel manganese oxide oxygen evolution reaction catalyst by operando Ni L-Edge X-ray absorption spectroscopy and 2p3d resonant inelastic X-ray scattering, ACS Appl. Mater. Interfaces 11 (2019) 38595–38605, https://doi.org/10.1021/acsami.9b06752.
[9] J. Juodkazytė, B. Šebeka, I. Savickaja, M. Petrulevičienė, S. Butkutė, V. Jasulaitienė, A. Selskis, R. Ramanauskas, Electrolytic splitting of saline water: Durable nickel oxide anode for selective oxygen evolution, Int J. Hydrog. Energy 44 (2019) 5929–5939, https://doi.org/10.1016/j.ijhydene.2019.01.120.
[10] M.I. Jamesh, Recent progress on earth abundant hydrogen evolution reaction and oxygen evolution reaction bifunctional electrocatalyst for overall water splitting in alkaline media, J. Power Sources 333 (2016) 213–236, https://doi.org/10.1016/j.jpowsour.2016.09.161.
[11] M. Gong, H. Dai, A mini review of NiFe-based materials as highly active oxygen evolution reaction electrocatalysts, Nano Res 8 (2014) 23–39, https://doi.org/10.1007/s12274-014-0591-z.
[12] R. Wu, Y. Dong, P. Jiang, G. Wang, Y. Chen, X. Wu, Electrodeposited synthesis of self-supported Ni-P cathode for efficient electrocatalytic hydrogen generation, Prog. Nat. Sci.: Mater. Int. 26 (2016) 303–307, https://doi.org/10.1016/j.pnsc.2016.05.014.
[13] M.I. Jamesh, Recent progress on earth abundant hydrogen evolution reaction and oxygen evolution reaction bifunctional electrocatalyst for overall water splitting in alkaline media, J. Power Sources 333 (2016) 213–236, https://doi.org/10.1016/j.jpowsour.2016.09.161.
[14] J.-W. Zhao, C.-F. Li, Z.-X. Shi, J.-L. Guan, G.-R. Li, Boosting lattice oxygen oxidation of perovskite to efficiently catalyze oxygen evolution reaction by FeOOH decoration, Research 2020 (2020) 1–15, https://doi.org/10.34133/2020/6961578.
[15] R. Bose, V.R. Jothi, D.B. Velusamy, P. Arunkumar, S.C. Yi, A highly effective, stable oxygen evolution catalyst derived from transition metal selenides and phosphides, Part. Part. Syst. Charact. 35 (2018) 1–9, https://doi.org/10.1002/ppsc.201800135.
[16] Z. Qiu, C.W. Tai, G.A. Niklasson, T. Edvinsson, Direct observation of active catalyst surface phases and the effect of dynamic self-optimization in NiFe-layered double hydroxides for alkaline water splitting, Energy Environ. Sci. 12 (2019) 572–581, https://doi.org/10.1039/c8ee03282c.
[17] N.K. Singh, R.N. Singh, Electrocatalytic properties of spinel type Ni(x)Fe(3-x)O4 synthesized at low temperature for oxygen evolution in KOH solutions, Indian, J. Chem. - Sect. A Inorg., Phys., Theor. Anal. Chem. 38 (1999) 491–495.
[18] C. Ma, S. Wang, F.C. Walsh, The electrodeposition of nanocrystalline Cobalt-Nickel-phosphorus alloy coatings: a review, Trans. Inst. Met. Finish. 93 (2015) 275–280, https://doi.org/10.1080/00202967.2015.1114729.
[19] W.J.F. Gannon, D.R. Jones, C.W. Dunnill, Enhanced lifetime cathode for alkaline electrolysis using standard commercial titanium nitride coatings, Processes 7 (2019), https://doi.org/10.3390/pr7020112.
[20] M. Gong, Y. Li, H. Wang, Y. Liang, J.Z. Wu, J. Zhou, J. Wang, T. Regier, F. Wei, H. Dai, An advanced Ni-Fe layered double hydroxide electrocatalyst for water oxidation, J. Am. Chem. Soc. 135 (2013) 8452–8455, https://doi.org/10.1021/ja4027715.
[21] J.W. Zhao, H. Zhang, C.F. Li, X. Zhou, J.Q. Wu, F. Zeng, J. Zhang, G.R. Li, Key roles of surface Fe sites and Sr vacancies in the perovskite for an efficient oxygen evolution reaction via lattice oxygen oxidation, Energy Environ. Sci. (2022), https://doi.org/10.1039/d2ee00264g.
[22] S.R. Mellsop, A. Gardiner, B. Johannessen, A.T. Marshall, Structure and transformation of oxy-hydroxide films on Ni anodes below and above the oxygen evolution potential in alkaline electrolytes, Electro Acta 168 (2015) 356–364, https://doi.org/10.1016/j.electacta.2015.04.020.
[23] A. Van der Ven, D. Morgan, Y.S. Meng, G. Ceder, Phase stability of nickel hydroxides and oxyhydroxides, J. Electrochem Soc. 153 (2006) A210, https://doi.org/10.1149/1.2138572.
[24] R. Farhat, J. Dhainy, L.I. Halaoui, Oer catalysis at activated and codeposited nife-oxo/hydroxide thin films is due to postdeposition surface-fe and is not sustainable without fe in solution, ACS Catal. 10 (2020) 20–35, https://doi.org/10.1021/acscatal.9b02580.
[25] M.W. Louie, A.T. Bell, An investigation of thin-film Ni-Fe oxide catalysts for the electrochemical evolution of oxygen, J. Am. Chem. Soc. 135 (2013) 12329–12337, https://doi.org/10.1021/ja405351s.
[26] O. Diaz-Morales, I. Ledezma-Yanez, M.T.M. Koper, F. Calle-Vallejo, Guidelines for the rational design of Ni-Based double hydroxide electrocatalysts for the oxygen evolution reaction, ACS Catal. 5 (2015) 5380–5387, https://doi.org/10.1021/acscatal.5b01638.
[27] M.B. Stevens, C.D.M. Trang, L.J. Enman, J. Deng, S.W. Boettcher, Reactive Fe-Sites in Ni/Fe (Oxy)hydroxide are responsible for exceptional oxygen electrocatalysis activity, J. Am. Chem. Soc. 139 (2017) 11361–11364, https://doi.org/10.1021/jacs.7b07117.
[28] F. Dionigi, Z. Zeng, I. Sinev, T. Merzdorf, S. Deshpande, M.B. Lopez, S. Kunze, I. Zegkinoglou, H. Sarodnik, D. Fan, A. Bergmann, J. Drnec, J.F. de Araujo, M. Gliech, D. Teschner, Z. Zhu, W.X. Li, J. Greeley, B.R. Cuenya, P. Strasser, In-situ structure and catalytic mechanism of NiFe and CoFe layered double hydroxides during oxygen evolution, Nat. Commun. 11 (2020) 1–10, https://doi.org/10.1038/s41467-020-16237-1.
[29] C.F. Li, L.J. Xie, J.W. Zhao, L.F. Gu, H.B. Tang, L. Zheng, G.R. Li, Interfacial Fe−O−Ni−O−Fe bonding regulates the active Ni Sites of Ni-MOFs via iron doping and decorating with FeOOH for super-efficient oxygen evolution, Angew. Chem. - Int. Ed. 61 (2022), https://doi.org/10.1002/anie.202116934.
[30] C.F. Li, L.J. Xie, J.W. Zhao, L.F. Gu, J.Q. Wu, G.R. Li, Interfacial electronic modulation by Fe2O3/NiFe-LDHs heterostructures for efficient oxygen evolution at high current density, Appl. Catal. B. 306 (2022), https://doi.org/10.1016/j.apcatb.2022.121097.
[31] D. Friebel, M.W. Louie, M. Bajdich, K.E. Sanwald, Y. Cai, A.M. Wise, M.J. Cheng, D. Sokaras, T.C. Weng, R. Alonso-Mori, R.C. Davis, J.R. Bargar, J.K. Nørskov, A. Nilsson, A.T. Bell, Identification of highly active Fe sites in (Ni,Fe)OOH for electrocatalytic water splitting, J. Am. Chem. Soc. 137 (2015) 1305–1313, https://doi.org/10.1021/ja511559d.

[32] L. Trotochaud, S.L. Young, J.K. Ranney, S.W. Boettcher, Nickel-Iron oxyhydroxide oxygen-evolution electrocatalysts: the role of intentional and incidental iron incorporation, J. Am. Chem. Soc. 136 (2014) 6744–6753, https://doi.org/ 10.1021/ja502379c.

[33] Q. Han, Y. Luo, J. Li, X. Du, S. Sun, Y. Wang, G. Liu, Z. Chen, Efficient NiFe-based oxygen evolution electrocatalysts and origin of their distinct activity, Appl. Catal. B. 304 (2022), 120937, https://doi.org/10.1016/j.apcatb.2021.120937.

[34] L. Peng, N. Yang, Y. Yang, Q. Wang, X. Xie, D. Sun-Waterhouse, L. Shang, T. Zhang, G.I.N. Waterhouse, Atomic cation-vacancy engineering of NiFe-layered double hydroxides for improved activity and stability towards the oxygen evolution reaction, Angew. Chem. - Int. Ed. 60 (2021) 24612–24619, https://doi.org/ 10.1002/anie.202109938.

[35] M.S. Ali Akbari, R. Bagheri, Z. Song, M.M. Najafpour, Oxygen-evolution reaction by nickel/nickel oxide interface in the presence of ferrate(VI, Sci. Rep. 10 (2020) 1–11, https://doi.org/10.1038/s41598-020-65674-x.

[36] C.B. Mullins, Y.J. Son, K. Kawashima, B.R. Wygant, C.H. Lam, J.N. Burrow, H. Celio, A. Dolocan, J.G. Ekerdt, Anodized nickel foam for oxygen evolution reaction in fe-free and unpurified alkaline electrolytes at high current densities, ACS Nano 15 (2021) 3468–3480, https://doi.org/10.1021/acsnano.0c10788.

[37] C. Hu, Y. Hu, C. Fan, L. Yang, Y. Zhang, H. Li, W. Xie, Surface-enhanced raman spectroscopic evidence of key intermediate species and role of nife dual-catalytic center in water oxidation, Angew. Chem. - Int. Ed. 60 (2021) 19774–19778, https://doi.org/10.1002/anie.202103888.

[38] Q. Kang, D. Lai, W. Tang, Q. Lu, F. Gao, Intrinsic activity modulation and structural design of NiFe alloy catalysts for an efficient oxygen evolution reaction, Chem. Sci. 12 (2021) 3818–3835, https://doi.org/10.1039/d0sc06716d.

[39] D. Zhou, P. Li, X. Lin, A. McKinley, Y. Kuang, W. Liu, W.F. Lin, X. Sun, X. Duan, Layered double hydroxide-based electrocatalysts for the oxygen evolution reaction: Identification and tailoring of active sites, and superaerophobic nanoarray electrode assembly, Chem. Soc. Rev. 50 (2021) 8790–8817, https://doi.org/ 10.1039/d1cs00186h.

[40] S.-Y. Lee, I.-S. Kim, H.-S. Cho, C.-H. Kim, Y.-K. Lee, Resolving potential-dependent degradation of electrodeposited Ni(OH)2 catalysts in alkaline oxygen evolution

reaction (OER): In situ XANES studies, Appl. Catal. B. 284 (2020), 119729, https:// doi.org/10.1016/j.apcatb.2020.119729.

[41] S.Y. Lee, S.J. Kim, W.J. Lee, Y.K. Lee, Boosting activity and durability of an electrodeposited Ni(OH)2catalyst using carbon nanotube-grafted substrates for the alkaline oxygen evolution reaction, ACS Appl. Nano Mater. 4 (2021) 10267–10274, https://doi.org/10.1021/acsanm.1c01766.

[42] D.K. Bediako, B. Lassalle-Kaiser, Y. Surendranath, J. Yano, V.K. Yachandra, D. G. Nocera, Structure-activity correlations in a nickel-borate oxygen evolution catalyst, J. Am. Chem. Soc. 134 (2012) 6801–6809, https://doi.org/10.1021/ ja301018q.

[43] Z. Lu, W. Xu, W. Zhu, Q. Yang, X. Lei, J. Liu, Y. Li, X. Sun, X. Duan, Three-dimensional NiFe layered double hydroxide film for high-efficiency oxygen evolution reaction, Chem. Commun. 50 (2014) 6479–6482, https://doi.org/ 10.1039/c4cc01625d.

[44] L. Trotochaud, S.L. Young, J.K. Ranney, S.W. Boettcher, Nickel-Iron oxyhydroxide oxygen-evolution electrocatalysts: the role of intentional and incidental iron incorporation, J. Am. Chem. Soc. 136 (2014) 6744–6753, https://doi.org/ 10.1021/ja502379c.

[45] J.M.P. Martirez, E.A. Carter, Noninnocent influence of host β-NiOOH redox activity on transition-metal dopants' efficacy as active sites in electrocatalytic water oxidation, ACS Catal. 10 (2020) 2720–2734, https://doi.org/10.1021/ acscatal.9b05092.

[46] Y. Zhuang, Y. Kong, Q. Liu, B. Shi, Alcohol-assisted self-assembled 3D hierarchical iron (hydr)oxide nanostructures for water treatment, CrystEngComm 19 (2017) 5926–5933, https://doi.org/10.1039/c7ce01320e.

[47] X. Zhang, L. An, J. Yin, P. Xi, Z. Zheng, Y. Du, Effective construction of high-quality iron oxy-hydroxides and co-doped iron oxy-hydroxides nanostructures: towards the promising oxygen evolution reaction application, Sci. Rep. 7 (2017) 1–10, https:// doi.org/10.1038/srep43590.

[48] J. Yan, L. Kong, Y. Ji, J. White, Y. Li, J. Zhang, P. An, S. Liu, S.T. Lee, T. Ma, Single atom tungsten doped ultrathin α-Ni(OH)2 for enhanced electrocatalytic water oxidation, Nat. Commun. 10 (2019) 1–10, https://doi.org/10.1038/s41467-019-09845-z.